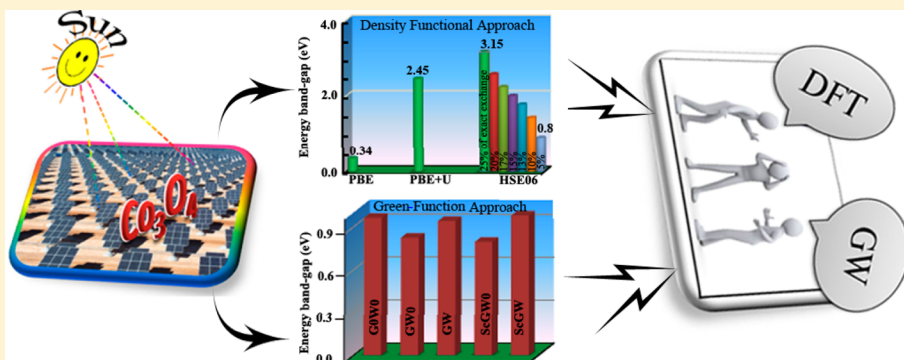


# Putting DFT to the Test: A First-Principles Study of Electronic, Magnetic, and Optical Properties of $\text{Co}_3\text{O}_4$

Vijay Singh, Monica Kosa, Koushik Majhi, and Dan Thomas Major\*

Department of Chemistry, the Lise Meitner-Minerva Center of Computational Quantum Chemistry, and the Institute for Nanotechnology and Advanced Materials, Bar-Ilan University, Ramat-Gan 52900, Israel

 Supporting Information



**ABSTRACT:** First-principles density functional theory (DFT) and a many-body Green's function method have been employed to elucidate the electronic, magnetic, and photonic properties of a spinel compound,  $\text{Co}_3\text{O}_4$ .  $\text{Co}_3\text{O}_4$  is an antiferromagnetic semiconductor composed of cobalt ions in the  $\text{Co}^{2+}$  and  $\text{Co}^{3+}$  oxidation states.  $\text{Co}_3\text{O}_4$  is believed to be a strongly correlated material, where the on-site Coulomb interaction ( $U$ ) on Co d orbitals is presumably important, although this view has recently been contested. The suggested optical band gap for this material ranges from 0.8 to 2.0 eV, depending on the type of experiments and theoretical treatment. Thus, the correlated nature of the Co d orbitals in  $\text{Co}_3\text{O}_4$  and the extent of the band gap are still under debate, raising questions regarding the ability of DFT to correctly treat the electronic structure in this material. To resolve the above controversies, we have employed a range of theoretical methods, including pure DFT, DFT+U, and a range-separated exchange–correlation functional (HSE06) as well as many-body Green's function theory (i.e., the GW method). We compare the electronic structure and band gap of  $\text{Co}_3\text{O}_4$  with available photoemission spectroscopy and optical band gap data and confirm a direct band gap of ca. 0.8 eV. Furthermore, we have also studied the optical properties of  $\text{Co}_3\text{O}_4$  by calculating the imaginary part of the dielectric function ( $\text{Im}(\epsilon)$ ), facilitating direct comparison with the measured optical absorption spectra. Finally, we have calculated the nearest-neighbor interaction ( $J_1$ ) between  $\text{Co}^{2+}$  ions to understand the complex magnetic structure of  $\text{Co}_3\text{O}_4$ .

## 1. INTRODUCTION

Most of today's growing energy consumption relies on nonrenewable and polluting energy sources such as petroleum, coal, natural gas, and nuclear power. Because of financial, geopolitical, and environmental concerns, considerable effort is being invested in searching for alternative energy conversion systems that are economical, renewable, clean, and efficient. Photovoltaic (PV) systems, which convert sunlight into either electrical or chemical energy, constitute a promising renewable energy source.<sup>1–5</sup> In PV cells, the photon-absorbing materials should exhibit optical absorptions in the visible range of the solar spectrum to maximize the efficiency.

Current state-of-the-art PV systems based on perovskites have reached impressive performance.<sup>6</sup> Nonetheless, because of high costs and safety issues of current technologies, the search for new cheap PV alternatives continues. One such family of potential PV materials is metal oxides.<sup>7,8</sup> Metal oxides are attractive semiconductor alternatives because of their abundance, low toxicity, ease of processing, and stability. Nonethe-

less, efficient metal-oxide-based PV cells with high power conversion efficiency have yet to be discovered.

Cobalt oxide,  $\text{Co}_3\text{O}_4$ , is a potential PV candidate with optical absorption in the visible region.<sup>9,10</sup> Additionally,  $\text{Co}_3\text{O}_4$  also exhibits intriguing chemical and catalytic properties. Therefore, it has great potential in novel renewable energy applications.<sup>9,11–17</sup>

From a theoretical point of view,  $\text{Co}_3\text{O}_4$  is a challenging material. As a normal spinel structure,  $\text{Co}_3\text{O}_4$  has two distinct Co sites in a two-formula-unit face-centered-cubic (FCC) primitive cell. One site is occupied by a  $\text{Co}^{2+}$  ion, which is surrounded by a tetrahedral  $\text{O}^{2-}$  coordination sphere (CoT), while another site is occupied by  $\text{Co}^{3+}$  ions and is in an octahedral environment (CoO) surrounded by six  $\text{O}^{2-}$  ions (Figure 1a). The electronic, magnetic, and optical properties of  $\text{Co}_3\text{O}_4$  have been studied by several groups, yet the correct

Received: August 26, 2014



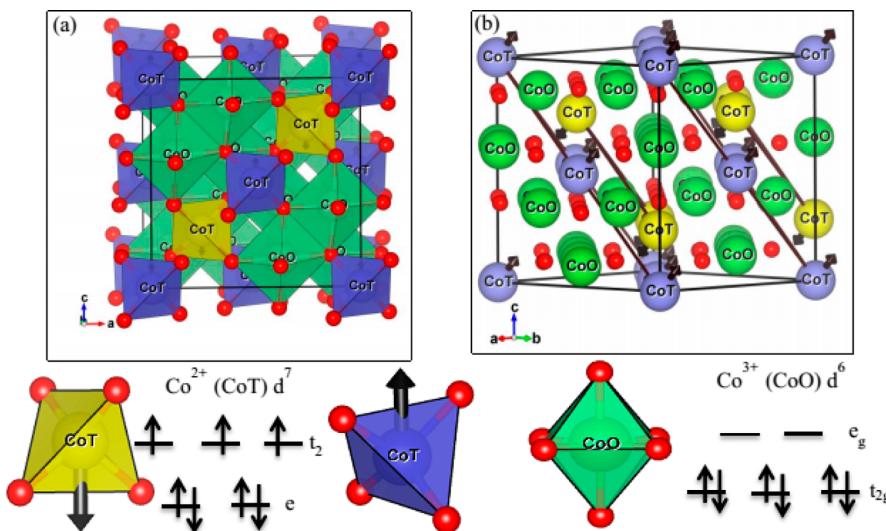


**Figure 1.** (a) Face-centered-cubic unit cell of  $\text{Co}_3\text{O}_4$  with two nonequivalent Co ions:  $\text{Co}^{2+}$  with tetrahedrally coordinated oxygens (CoT) and  $\text{Co}^{3+}$  with octahedrally coordinated oxygens (CoO). (b) Model magnetic structure of  $\text{Co}_3\text{O}_4$ , where CoT (blue and yellow spheres) located in the [111] plane interact antiferromagnetically. (bottom) Schematic diagram showing the expected crystal field splittings of (left) a  $\text{Co}^{2+}$  ion in a tetrahedral field and (right) a  $\text{Co}^{3+}$  ion in an octahedral field.

electronic structure and the energy band gap are still under debate. It has been found experimentally that the tetrahedrally coordinated  $\text{Co}^{2+}$  ion has a magnetic moment of  $3.20\mu_B$ , slightly more than the expected spin-only value of  $3\mu_B$ . In contrast,  $\text{Co}^{3+}$  is diamagnetic in nature. Therefore, the magnetic properties of  $\text{Co}_3\text{O}_4$  are governed by the  $\text{Co}^{2+}$  ions, which are located in the [111] plane of the unit cell (Figure 1b). The planes of  $\text{Co}^{2+}$  ions are arranged antiferromagnetically, and this has been explained by a superexchange mechanism via intervening oxygens.<sup>18–20</sup> Interestingly, in spite of the significant efforts invested in computing the fundamental band gap of  $\text{Co}_3\text{O}_4$ , the band gap and the detailed electronic structure of this material are not yet fully understood.<sup>21,22</sup> Importantly, many features of transition-metal oxides, such as their electronic, magnetic, and optical properties, are difficult to treat theoretically because of the complex electronic structure of these materials.<sup>23–25</sup> In the following we will present a brief overview of some of the considerable work performed for this material.

X-ray photoelectron spectroscopy (XPS) is often used to study the electronic structure and composition of transition-metal oxides. Chung et al.<sup>26</sup> measured the XPS spectrum of  $\text{Co}_3\text{O}_4$  and assigned the structure of the valence band, which arises mainly from  $\text{Co}^{3+}$  3d  $t_{2g}$  states with a peak at  $\sim 1$  eV below the Fermi level and  $\text{Co}^{2+}$  3d  $e$  and  $t_2$  states with peaks in the  $\sim 2$ – $4$  eV region. Moreover, the O 2p peak is located in the range  $\sim 5$ – $7$  eV, far from the Fermi level. Jugnet and Duc<sup>27</sup> performed a comparative study of CoO and  $\text{Co}_3\text{O}_4$  using both XPS and ultraviolet photoelectron spectroscopy (UPS). The advantage of UPS is its ability to measure the total density of the occupied states rather accurately, although the method is limited to valence-electron energy levels. The work of Jugnet and Duc<sup>27</sup> largely agrees with that of Chung et al.,<sup>26</sup> although the authors found an additional weak peak above the  $\text{Co}^{3+}$  3d  $t_{2g}$  state, proximal to the Fermi level. It was suggested that this peak arises from  $\text{Co}^{2+}$  3d  $e$  states. Recently, Qiao et al.<sup>9</sup> performed a careful valence-band *in situ* XPS study and confirmed the obtained UPS spectrum of  $\text{Co}_3\text{O}_4$ . However, in that work no detailed orbital assignment was attempted for the

Co states. Several optical spectra dealing with the excited-state properties of  $\text{Co}_3\text{O}_4$  have also been presented. Tanaka<sup>28</sup> obtained the absorption coefficient and refractive index for  $\text{Co}_3\text{O}_4$ . Highly intense absorption maxima were observed at 400 nm (3.10 eV) and 750 nm (1.65 eV). Intriguingly, in the tail of the absorption spectrum one may spot a small yet significant peak at  $\sim 1100$  nm (1.10 eV). Belova et al.<sup>29</sup> confirmed the existence of the aforementioned peak using optical transmission spectroscopy and placed it below 1.05 eV. Additionally, these authors also observed an additional intense peak at around 400 nm (5.39 eV). Cheng et al.<sup>30</sup> performed optical absorption edge analysis and found that the minimum band-gap energies of 1.50 and 1.52 eV correspond to the edge of the charge transfer band ( $\text{Co}^{3+}\text{--Co}^{2+}$ ). This finding has also received support from Barreca et al.<sup>31</sup> using visible–near-IR (NIR) absorption spectroscopy. In view of the above, Martens et al.<sup>32</sup> studied the optical transition in  $\text{Co}_3\text{O}_4$  by following the change in the dielectric function through spectroscopic ellipsometry, and indeed, they observed transitions at 0.80, 1.60, 2.65, and 4.40 eV. Subsequently, Kim and Park<sup>33</sup> measured the dielectric function of  $\text{Co}_3\text{O}_4$ , which exhibits absorption structures at 1.65, 2.4, and 2.8 eV. Recently, a similar experiment was performed by Qiao et al.,<sup>9</sup> who obtained results in agreement with Kim and Park.<sup>33</sup> However, in contrast to some of the above findings, infrared optical spectroscopy demonstrated evidence for a direct fundamental band gap of 0.76 eV in the NIR.<sup>9</sup> Interestingly, a recent study of long-lived photoexcited carrier dynamics of d–d excitations in  $\text{Co}_3\text{O}_4$  has suggested the optical band gap to be 0.82 eV.<sup>34</sup> Thus, a plethora of experimental values exist for the electronic transitions in  $\text{Co}_3\text{O}_4$ .

Several theoretical studies have addressed the electronic details of  $\text{Co}_3\text{O}_4$  to resolve the above discrepancies. Belova et al.<sup>29</sup> used the SCF  $X_\alpha$ -SW method to understand the obtained optical spectrum of  $\text{Co}_3\text{O}_4$ , while a semiempirical molecular orbital approach was employed by Miedzinska et al.<sup>35</sup> to construct the absorption spectra. However, these calculations led to different interpretations of the optical spectrum of  $\text{Co}_3\text{O}_4$ . For example, according to Belova et al., the

experimentally observed peak at 2.85 eV is a d–d transition, while Miedzinska et al. suggested it to be a p–d transition. Walsh et al.<sup>21</sup> employed a projector augmented wave (PAW) basis set in conjunction with the PBE+U functional, where  $U = 2$  eV for both  $\text{Co}^{2+}$  and  $\text{Co}^{3+}$  3d orbitals. These authors found a minimum direct optical band gap of 1.23 eV at the X point of the Brillouin zone (BZ), although the obtained density of states (DOS) did not give an antiferromagnetic (AFM) ground state because of asymmetry in the up and down DOS. Subsequently, Xu et al.<sup>36</sup> performed PBE calculations using a double-numerical basis set and obtained a minimal direct band gap of 1.75 eV at the X point of the BZ. Chen et al.<sup>22</sup> combined the PBE functional with an effective on-site potential,  $\text{PBE}+\text{U}_{\text{eff}}$ , where  $\text{U}_{\text{eff}} = U - J$ , in which  $U$  is the Coulomb interaction and  $J$  is the intra-atomic Hund's exchange between localized electrons. In this work, two sets of  $\text{U}_{\text{eff}}$  were employed (4.4 eV for  $\text{Co}^{2+}$  and 6.7 eV for  $\text{Co}^{3+}$ ), and the results obtained using the  $\text{PBE}+\text{U}_{\text{eff}}$  functional were compared with calculations using the hybrid PBE0 functional. These authors concluded that the hybrid PBE0 functional overestimates the band gap and proposed a minimum band gap of 1.96 eV at the X point of the BZ using  $\text{PBE}+\text{U}_{\text{eff}}$ . However, the computed electronic structure is seemingly at odds with the measured experimental photoemission spectra, where the O 2p and Co d states are well-separated by a distinct energy interval. Instead, Chen and co-workers obtained an electronic structure exhibiting strong hybridization of the O 2p and Co 3d states (both  $\text{Co}^{2+}$  and  $\text{Co}^{3+}$ ). Recently, Qiao et al.<sup>9</sup> performed DFT calculations with a range of different values of  $\text{U}_{\text{eff}}$ . The authors presented a two-dimensional contour mapping of the calculated DOS as a function of different  $\text{U}_{\text{eff}}$  values of both  $\text{Co}^{2+}$  and  $\text{Co}^{3+}$  ions. The authors concluded that the most probable band gap, computed with  $\text{U}_{\text{eff}} = 0$ , is located at 0.34 eV at the X point of the BZ. On this basis, they argued that  $\text{Co}_3\text{O}_4$  does not exhibit strong Coulomb correlations. We note that in spite of the seemingly good agreement between the electronic structures obtained with the pure PBE functional and experiment, this functional is known to underestimate the band gap of semiconductor materials in general.<sup>37</sup> Recently, Lima<sup>38</sup> employed the B3PW91 hybrid functional and suggested this DFT flavor gives better results than other schemes, with a proposed fundamental gap of 1.55 eV. Lima also suggested an optical absorption spectrum by calculating the dielectric function and surprisingly identified a transition at 1.65 eV as a charge transfer between  $\text{Co}^{2+}$  and  $\text{Co}^{3+}$  ions. In contrast, experimentally, Waegele et al.<sup>34</sup> and Qiao et al.<sup>9</sup> assigned the above transition to be between  $\text{Co}^{3+}$  and  $\text{Co}^{2+}$  ions. In summary, the nature of the electronic and optical properties of  $\text{Co}_3\text{O}_4$  is still under debate, and it is clear that the computed band gap strongly depends on the choice of DFT method.

In the current work, we employed a range of first-principles DFT calculations, including PBE,  $\text{PBE}+\text{U}_{\text{eff}}$ , and the range-separated exchange–correlation functional HSE06. This functional was shown to capture the correct band-gap energy in several metal oxides.<sup>39</sup> We also used the many-body Green's function technique, known as the GW method, where  $G$  is the one-particle Green's function and  $W$  is a dynamically screened Coulomb interaction.<sup>40</sup> In the current study, we address the open question of whether the  $\text{Co}_3\text{O}_4$  band gap is located in the NIR (from 1.24 meV to 1.70 eV) or in the visible region (from 1.70 to 3.30 eV) and the correlated nature of this material.

## 2. METHODS AND COMPUTATIONAL DETAILS

**2.1. PBE,  $\text{PBE}+\text{U}_{\text{eff}}$ , and HSE06 Calculations.** All of the calculations were performed using the Vienna Ab Initio Simulation Package (VASP), which is a plane-wave implementation of DFT.<sup>41–43</sup> The valence electrons were described in terms of Kohn–Sham (KS) single-electron orbitals, which were expanded in a plane-wave basis with an energy cutoff of 500 eV. Core electrons were defined within the PAW methodology, and  $\Gamma$ -point-centered  $k$ -point meshes were used for all of the calculations. The  $k$ -point grid was  $8 \times 8 \times 8$  for all of the PBE and  $\text{PBE}+\text{U}_{\text{eff}}$  calculations. However, for the calculations with the HSE06 hybrid functional, we employed a  $\Gamma$ -point-centered  $4 \times 4 \times 4$   $k$ -point mesh because of the significant increase in the computational cost for computations with exact exchange.<sup>44</sup> BZ integration was done by the tetrahedron method with Blöchl corrections.<sup>45</sup> For the hybrid HSE06 calculations, the BZ was integrated using Gaussian smearing with a smearing width of 0.01 eV. In the  $\text{PBE}+\text{U}_{\text{eff}}$  calculations, the onsite Coulomb interaction  $\text{U}_{\text{eff}}$  was 4.4 eV for the  $\text{Co}^{2+}$  ions and 6.4 eV for the  $\text{Co}^{3+}$  ions.<sup>30,46</sup> All of the atoms were allowed to relax until the net force per atom was less than 0.01 eV/Å. Moreover, within the HSE06 approach several values of exact Hartree–Fock (HF) nonlocal exchange ( $\alpha$ ) were attempted: 25%, 20%, 17%, 15%, 13%, 10%, and 5%.<sup>47</sup> The screening parameter (which controls the extent of the range of the exchange interactions) was also tuned for two values of  $\alpha$  (5% and 25%)<sup>48</sup> to check the reliability of the calculations (Figures S1 and S2 in the Supporting Information).

To investigate the discrepancy between the fundamental band gap and the optical band gap, optical properties were also calculated in the PAW framework using the method of Gajdoš et al.<sup>49</sup> The imaginary part of the macroscopic dielectric tensor is directly related to the optical absorption spectrum of any material.<sup>50,51,58</sup> In addition to the optical properties, we also performed chemical-bonding analysis by plotting the crystal orbital Hamiltonian populations (COHPs)<sup>52–54</sup> for both spin densities of  $\text{Co}_3\text{O}_4$  for the  $\text{Co}^{2+}/\text{Co}^{3+}$ –O nearest-neighbor bonds. This new scheme has been implemented in the LOBSTER program, which calculates COHPs directly from the plane waves.<sup>54</sup> The COHP provides an energy-resolved visualization of the chemical bonding in solids based on DFT calculations by rewriting the band-structure energy as the sum of energies per orbital contribution. The energy integral of COHP (ICOHP) gives access to the contribution of an atom or a chemical bond to the distribution of the one particle energy. The validity of the method has previously been shown by application to chemical textbook examples such as diamond, GaAs, CsCl, and Na and several different classes of solid-state materials.<sup>52,53,55,54</sup>

**2.2. Many-Body Green's Function Calculations Using the GW Approximation.** To further validate the present calculations, we adopted Green's function theory based on the GW approximation. The GW approximation, originally formulated by Hedin, uses the many-body Green's function to solve the quasiparticle (QP) equation, with a perturbative expansion of the frequency-dependent nonlocal self-energy operator ( $\Sigma(\mathbf{r}, \mathbf{r}', \omega)$ ).<sup>40,56</sup> It has been applied primarily to conventional semiconductor solids to calculate band-gap energies and band structures.<sup>57,58</sup> Application of the GW approximation requires input of initial-guess QP energies and wave functions, which are usually taken from KS-DFT.<sup>59,60</sup> Therefore, the GW approximation has also been called a

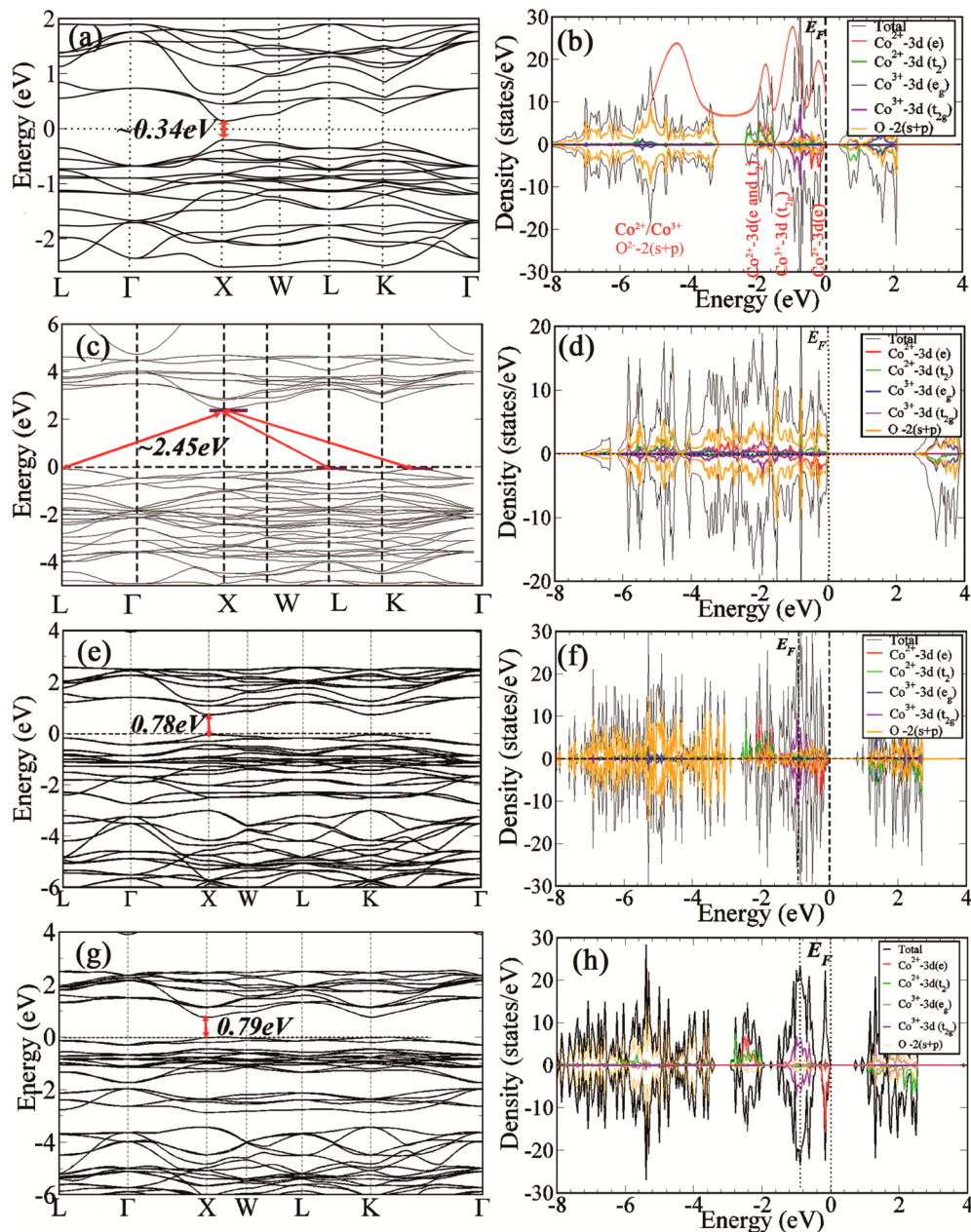


**Figure 2.** Calculated (a, c, e, g) total band structures and (b, d, f, h) total and partial densities of states for  $\text{Co}_3\text{O}_4$  using (a, b) the PBE functional; (c, d) the PBE+ $U_{\text{eff}}$  functional with  $U_{\text{eff}} = U - J = 4.4$  and 6.7 eV for  $\text{Co}^{2+}$  and  $\text{Co}^{3+}$ , respectively; (e, f) the HSE06 functional with a 5% short-range HF exchange, and (g, h) the Sc-GW0 method, which gave the best performance among all the GW methods. A schematic representation of the experimental electronic structure of  $\text{Co}_3\text{O}_4$  obtained from photoemission spectroscopy is shown in (b).

perturbation theory improvement to DFT. The QP band gap predicted by the GW approximation is the theoretical equivalent of the gap derived from photoemission spectroscopy (PES) and inverse photoemission spectroscopy (IPES), in which the total number of electrons decreases and increases after the measurement, respectively.<sup>56</sup> In the present work, the QP calculations were performed using a perturbative non-self-consistent GW method (G0W0) as well as the much more expensive self-consistent GW approach.<sup>60</sup> Within the self-consistent GW approach, we adopted two strategies. The first one was the “energy-only” self-consistent approach, in which the eigenvalues are updated only in  $G$  (i.e., GW0) or in both  $G$  and  $W$  (i.e., GW) while the QP wave functions are kept fixed at the KS ones.<sup>61,58</sup> The other approach was the QP self-

consistent GW (QSGW) method, in which the QP eigenvalues and wave functions are both updated either in  $G$  (Sc-GW0) or both  $G$  and  $W$  (Sc-GW).<sup>62,57,63,59,64</sup> In the present work, we performed systematic tests of various forms of the GW method for  $\text{Co}_3\text{O}_4$ . The input wave functions and energies for the G0W0 calculation were obtained from DFT calculations on the bulk unit cell using the PBE, PBE+ $U_{\text{eff}}$ , and HSE06 ( $\alpha = 5\%$ ) functionals. The corresponding G0W0 calculations will henceforth be denoted as  $\text{G0W0}_{\text{PBE}}$ ,  $\text{G0W0}_{\text{PBE+}U_{\text{eff}}}$ , and  $\text{G0W0}_{\text{HSE06}}$ . A  $4 \times 4 \times 4$   $\Gamma$ -point-centered  $k$ -point mesh was used in the G0W0 calculation. The calculation of the response function used a  $\Gamma$ -point-centered  $2 \times 2 \times 2$   $q$ -point mesh. The converged numbers of bands and frequency points were 320 and 90, respectively. These settings gave QP gaps that were

converged to within 0.1 eV. In the GW approximation, the screened Coulomb interaction,  $W$ , was calculated within the random-phase approximation (RPA). The RPA approximation captures the local field force, which is a local Coulomb field, linked with the quasiparticle.<sup>40</sup> Moreover, the local field can be approximated either by including the change in the Hartree potential or by including both the Hartree and exchange–correlation potentials (RPA-DFT). We employed both approaches, but only the RPA-DFT results are shown in the Results and Discussion. For calculation of the band structure of  $\text{Co}_3\text{O}_4$ , Wannier functions were used to interpolate the initially calculated many-body band structure from the coarse mesh of the BZ point to the usual symmetry lines using the Wannier90 code.<sup>65</sup> Finally, the frequency-dependent macroscopic dielectric function was calculated with the RPA for  $\text{Co}_3\text{O}_4$ . It can also be directly related to the optical absorption spectrum.

### 3. RESULTS AND DISCUSSION

**3.1. Electronic Structure and Band Gap.** Initially, we examined the position of the KS valence-band maxima (VBM) and conduction-band minima (CBM) obtained using DFT and compared the computed electronic structure with the experimental PES of Jugnet and Duc<sup>27</sup> and Qiao et al.<sup>9</sup> Using the PBE functional, we obtained a direct band gap (at the X point of the BZ) of ca. 0.34 eV, as shown in Figure 2a, in agreement with Qiao et al.<sup>9</sup> We note that the PBE functional typically underestimates the band gap in semiconductors.<sup>66</sup> For convenience, we divide the electronic band structure into four regions: (1)  $\text{Co}^{2+}$  3d e states, (2)  $\text{Co}^{3+}$  3d  $t_{2g}$  states, (3)  $\text{Co}^{2+}$  3d e and  $t_2$  states, and (4) a mixture of O 2p and  $\text{Co}^{2+}/\text{Co}^{3+}$  electronic states (see Figure 2b). Inspection of the DOS computed with the pure PBE functional reveals that the computed electronic structure is close to the experimental valence-band PES (Figure 2b).<sup>9</sup> Thus, PBE predicts a good DOS, although it underestimates the band gap. It is instructive to analyze the  $\text{Co}_3\text{O}_4$  electronic structure in light of what would be expected on the basis of standard crystal field theory. A schematic diagram of the expected crystal field splittings for  $\text{Co}^{2+}$  and  $\text{Co}^{3+}$  is shown in Figure 1. According to crystal field theory, the  $\text{Co}^{2+}$  3d orbital degeneracy breaks into doubly degenerate low-energy 3d e states containing the  $d_{x^2-y^2}$  and  $d_z^2$  orbitals and triply degenerate high-energy 3d  $t_2$  states containing the  $d_{xy}$ ,  $d_{yz}$ , and  $d_{xz}$  orbitals. In this case, traditional crystal field prediction does not hold, as has been discussed by Chen et al.<sup>22</sup> Indeed, it is clear from the density of states that the Hund spin exchange (spin flip) energy (ca. >2 eV) is larger than the crystal field splitting for the  $\text{Co}^{2+}$  3d orbitals, and consequently, the high-spin quartet state is obtained. The minority spin channel of the  $\text{Co}^{2+}$  states is populated by 3d e states only and gives rise to a local magnetic moment of  $2.3\mu_B$ , which is  $\sim 0.9\mu_B$  less than the measured value of  $3.2\mu_B$ .<sup>18</sup> Such underestimation is typical for the PBE functional.<sup>67–69</sup> In comparison, the  $\text{Co}^{3+}$  ions are located in an octahedral environment of  $\text{O}^{2-}$  ions and exhibit strong crystal field splitting. The 3d orbitals split into doubly degenerate 3d  $e_g$  states ( $d_{x^2-y^2}$  and  $d_z^2$  orbitals) and triply degenerate 3d  $t_{2g}$  states ( $d_{xy}$ ,  $d_{yz}$ , and  $d_{xz}$  orbitals). The 3d  $e_g$  states are unoccupied, as they are located largely above the Fermi level, while the 3d  $t_{2g}$  states are close to the Fermi level. In this case the crystal field splitting is larger than the Hund exchange effect, and these octahedral centers exhibit low-spin states and remain diamagnetic.

In the valence region, the position of the tetrahedrally coordinated  $\text{Co}^{2+}$  3d e states in the minority spin channel, which are surprisingly well above the  $\text{Co}^{2+}$  3d  $t_2$  up states, presents a puzzling anomaly in the  $\text{Co}_3\text{O}_4$  electronic structure. We performed a chemical bond analysis to further dissect the effects at play in this material. To this end, in Figure 3 we

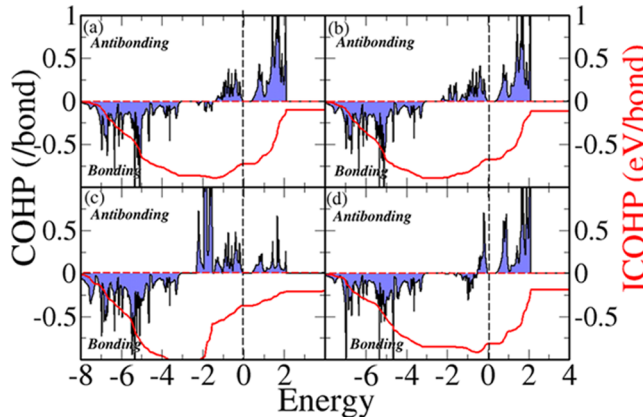


**Figure 3.** Off-site COHPs and ICOHPs (red) per bond for  $\text{Co}_3\text{O}_4$  for nearest neighbors of (a) spin-up  $\text{Co}^{3+}$ –O, (b) spin-down  $\text{Co}^{3+}$ –O, (c) spin-up  $\text{Co}^{2+}$ –O, and (d) spin-down  $\text{Co}^{2+}$ –O. All energies are relative to the Fermi energy.

display the off-site COHPs and ICOHPs per bond for the nearest neighbors of  $\text{Co}^{2+}$ –O and  $\text{Co}^{3+}$ –O interactions for both spin channels. The bonding contribution is indicated by a negative COHP and the antibonding contribution by a positive COHP. From the COHP plot in Figure 3a,b we find strong covalency between  $\text{Co}^{3+}$ –O pairs, as revealed by the ICOHP at the Fermi level, which is  $-0.72$  eV for the spin-up channel and  $-0.68$  eV for the spin-down channel. In contrast, for the  $\text{Co}^{2+}$ –O pairs we observe a significant difference between the different spin channels (Figure 3c,d). The spin-up channel has an ICOHP at the Fermi level of  $-0.44$  eV, while the spin-down channel has an ICOHP of  $-0.88$  eV. Noticeably, the calculated partial DOS suggests that the spin-down channel of  $\text{Co}^{2+}$ , corresponding to 3d e states (Figure 2b), is largely hybridized with valence oxygen states, and this bonding is indeed reflected in the ICOHP.

Furthermore, we probed the possibility of strong correlation, i.e., whether the on-site correlation  $U$  is significantly larger than the kinetic energy ( $T$ ) of the electrons ( $U/T \gg 1$ ). Thus, we performed PBE+ $U_{\text{eff}}$  calculations based on the formalism of Dudarev et al.<sup>70</sup> It is well-established that the magnitude of the  $U_{\text{eff}}$  parameter affects the binding and localization of the electrons in transition metals. Here we used the optimized values of  $U_{\text{eff}}$  for  $\text{Co}^{2+}$  (4.4 eV) and  $\text{Co}^{3+}$  (6.7 eV) as suggested by Qiao et al.<sup>9,22,46</sup> Using these Hubbard  $U$  parameters, we obtained an anticipated increase in the band gap of  $\text{Co}_3\text{O}_4$  with a value of 2.45 eV (Figure 2c). However, it is difficult to assign the band-gap type for  $\text{Co}_3\text{O}_4$  (i.e., direct or indirect), as the valence-band eigenvalue at the high-symmetry X point of the BZ is almost degenerate with the high-symmetry L point of the VBM. Interestingly, the obtained electronic structure is very similar to the DOS proposed by Chen et al.<sup>22</sup> and Qiao et al.<sup>9</sup> but does not agree well with the experimental PES spectra (Figure 2d). Particularly visible is the shift in the position of the O 2p states, which experimentally are rather far from the Fermi level (ca. 5–7 eV) but using PBE+ $U_{\text{eff}}$  are spread out in the

range 0–6 eV. Thus, the opening of the band gap has an accompanying change in the DOS for this material.

To further probe the electronic structure and energetic properties of  $\text{Co}_3\text{O}_4$ , we also employed the range-separated hybrid functional HSE06<sup>44</sup> with a screening parameter of 0.2 Å<sup>-1</sup> and varying amounts of HF exchange. We observed a linear dependence of the  $\text{Co}_3\text{O}_4$  band gap on the mixing strength of the short-range (SR) component of the PBE exchange with SR HF exchange ( $\alpha$ ) (Figure S3 in the Supporting Information). Upon comparison with the experimental XPS and UPS data,<sup>9,26,27</sup> we conclude that the optimal electronic structure is obtained with a small amount of SR HF exchange ( $\alpha \approx 5\%$ ; Figure 2e). The corresponding band gap is direct (at the X point of the BZ) with a value of ~0.78 eV (Figure 2f). Electronic structures corresponding to other values of the mixing parameter  $\alpha$  are presented in Figure S4 in the Supporting Information. A large mixing value of  $\alpha = 25\%$ , which is the standard value obtained by perturbation theory,<sup>71</sup> gives an electronic structure very similar to PBE+U<sub>eff</sub>. Again, the DOS obtained with a larger HF exchange component results in a deterioration of the electronic structure compared with the XPS and UPS data.<sup>9,26,27</sup>

To facilitate a more direct comparison with experiment, we also calculated the frequency-dependent macroscopic dielectric function using the independent-particle approximation (non-interacting particle–hole pairs). For the PBE and HSE06 ( $\alpha = 5\%$ ) functionals (Figure 4a,c), the calculated absorption

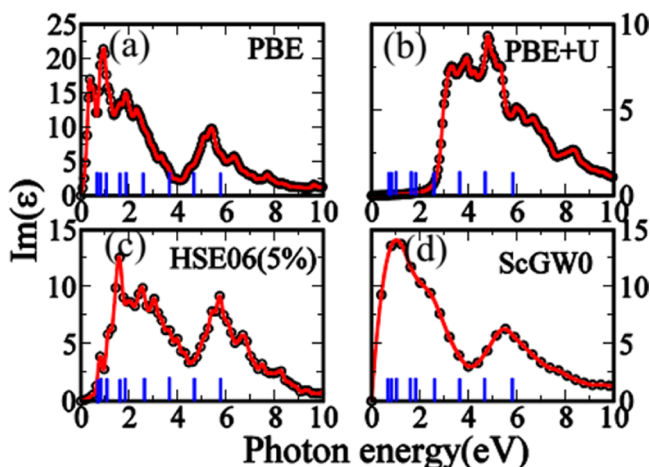


**Figure 4.** Calculated imaginary part of the macroscopic dielectric constant of  $\text{Co}_3\text{O}_4$  (black solid circles) for different approaches: (a) PBE; (b) PBE+U<sub>eff</sub>; (c) HSE06 ( $\alpha = 5\%$ ); (d) the best-fit GW (ScGW0) method. Experimentally observed absorption peaks are shown as blue bars.<sup>9</sup>

spectrum (i.e., the imaginary part of the macroscopic dielectric function) is in good agreement with experiment,<sup>9</sup> where absorption of low-energy photons is seen. In contrast, only absorption of short-wavelength, high-energy photons (>2 eV) is seen for the PBE+U<sub>eff</sub> functional (Figure 4b) and the HSE06 ( $\alpha = 25\%$ ) functional (Figure S5d in the Supporting Information).

Finally, to simulate the transition energies of  $\text{Co}_3\text{O}_4$  obtained in PES and IPES experiments, we calculated the QP gap using the GW method.<sup>56</sup> In practical GW calculations, the initial guesses for the energy and the wave function, which are used as input for G0W0, are crucial. In this work, we employed the eigenvalues and eigenfunctions from GGA calculations with the

PBE functional, as these gave the electronic structure in best agreement with the available PES spectra, as discussed above. Other possible initial guesses were also explored (e.g., G0W0<sub>PBE+U<sub>eff</sub></sub> and G0W0<sub>HSE06</sub>; Figure S6 in the Supporting Information). In addition to the non-self-consistent GW method, G0W0, we also employed additional approaches: partially self-consistent in  $G$  (GW0), partially self-consistent in both  $G$  and  $W$  (GW), fully self-consistent in  $G$  (Sc-GW0), and fully self-consistent in both  $G$  and  $W$  (Sc-GW). The GW results are summarized in Table S1 in the Supporting Information. Interestingly, the QP band gap is relatively insensitive to the level of GW approximation employed (Figure 5). The

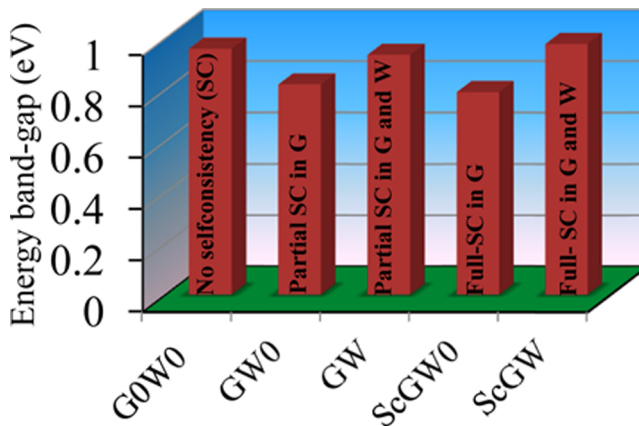


**Figure 5.** Calculated band-gap energies for  $\text{Co}_3\text{O}_4$  using different levels of the many-body Green's function GW approximation. The type of self-consistency is written along the bar for each method.

electronic structures at the various levels of GW theory are also rather similar, although some differences exist. Our calculations reveal that updating  $G$  only by partial self-consistent updating schemes (GW0 and GW) introduces some artifacts into the DOS. With these approximations, the position of the O 2p states shifts somewhat too far toward the core (8–10 eV), in disagreement with the experimental PES measurements (5–6 eV) (see Figure S7b,c in the Supporting Information). It has been suggested previously that GW0 for d states of metals may lead to errors.<sup>58</sup> The computed band gap is indirect ( $\Gamma$ –X) with values of 0.82 and 0.94 eV for GW0 and GW, respectively (Figure S8b,c in the Supporting Information). In comparison, one-shot GW (G0W0), Sc-GW0, and Sc-GW produce reasonable electronic structures (Figure S7a–c, respectively) that are in very good agreement with the PES spectra, and the corresponding band gaps are 0.98 eV (indirect  $\Gamma$ –X), 0.79 eV (direct at the X point of the BZ), and 0.98 eV (indirect  $\Gamma$ –X), respectively (Figure S8a–c). These values may be compared with the value reported by Qiao et al.,<sup>9</sup> who suggested  $\text{Co}_3\text{O}_4$  to be a weakly correlated material with a fundamental gap of 0.76 eV. In Figure 2g,h we show the best-fit Green's function band structure and DOS, obtained with Sc-GW0, which is further confirmed by the computed optical absorption (see below).

In view of the above, we calculated the GW frequency-dependent dielectric function using RPA and compared the imaginary part of the macroscopic dielectric function ( $\text{Im}(\epsilon)$ ) with the optical absorption spectrum. The imaginary part of the macroscopic dielectric tensor is directly related to the optical absorption spectrum of the material and can be computed with knowledge of the electronic band structure, as discussed by

Gajdoš et al.<sup>49</sup> We compare our results with the absorption peaks for  $\text{Co}_3\text{O}_4$  obtained by Qiao et al.,<sup>9</sup> shown as red bars in Figure S10 in the Supporting Information. The calculated absorption spectra for GW0 and GW seemingly have anomalous features corresponding to the O 2p electrons, similar to the problems associated with the DOS (Figure S10b,c). Indeed, the short-wavelength tail of the absorption spectrum is far from the measured absorption spectrum. In contrast, G0W0, Sc-GW0, and Sc-GW all reproduce the experimental spectrum reasonably well. Since the onsets of the peaks are not well-defined, the positions at the half-peak height are used for comparison (Figure S10). We find that the absorption tails for G0W0, Sc-GW0, and Sc-GW are in the ranges  $\sim 4.8\text{--}6$ ,  $\sim 4.8\text{--}6.2$ , and  $\sim 5.8\text{--}6.8$  eV, respectively (see Figure S10a–c). The experimental absorption peak (interband transition from O 2p to metal 3d absorption<sup>9</sup>) is located in the tail region at  $\sim 4.7\text{--}5.8$  eV. G0W0 and Sc-GW0 seem to fit this best. Considering the good agreement using the Sc-GW0 approach for the band gap (0.79 and 0.76/0.82 eV) and the magnetic moment ( $2.56\mu_{\text{B}}$  and  $3.20\mu_{\text{B}}$ ) as well, we adopt this method as the optimal one for  $\text{Co}_3\text{O}_4$ . The imaginary part of the dielectric function ( $\text{Im}(\epsilon)$ ) obtained using the Sc-GW0 method is shown in Figure 4d and compared with the DFT levels tested herein.

**3.2. Magnetic Properties.**  $\text{Co}_3\text{O}_4$  is a paramagnetic semiconductor at room temperature, and it undergoes an AFM transformation below the Néel temperature ( $T_N$ ) of  $\sim 40$  K. A neutron diffraction study claimed that all of the magnetic  $\text{Co}^{2+}$  ions, which reside in the [111] plane, interact antiferromagnetically.<sup>18</sup> However, the strength of the AFM interaction is weak, (i.e., 4–7 K).<sup>18,20,72</sup> Additionally, in the employed unit cell, each spin-up  $\text{Co}^{2+}$  ion has four tetrahedrally coordinated nearest-neighbor  $\text{Co}^{2+}$  ions with the spin-down configuration (Figure 6 inset). To quantify the strength of the

where  $i$  and  $j$  denote the nearest-neighbor sites. The number of such sites is 4 for a given unit cell. Therefore,  $J_1$  is expressed as

$$J_1 = \frac{1}{2} \times \frac{1}{4} \times \frac{1}{S^2} (E_{\text{AFM}} - E_{\text{FM}}) \quad (2)$$

where  $S = 3/2$  because each  $\text{Co}^{2+}$  ion has three unpaired electrons.

The calculated magnetic moment for a  $\text{Co}^{2+}$  ion is  $2.28\mu_{\text{B}}$  with the PBE functional, which underestimates the value of the magnetic moment and consequently overestimates  $J_1$ . On the other hand, the partial corrections of the PBE delocalization error with PBE+U<sub>eff</sub> and HSE06 improve the value of  $J_1$  significantly with respect to the experimental value (Figure 6). The computed magnetic moments using PBE+U<sub>eff</sub> and HSE06 ( $\alpha = 25\%$ ) are  $2.71\mu_{\text{B}}$  and  $2.66\mu_{\text{B}}$ , respectively. Consequently, the value of  $J_1$  is reduced drastically, resulting in better agreement with experiment for these functionals. However, as noted earlier, the electronic structures obtained using these functionals do not match the experimental XPS and UPS data as well as that obtained using the PBE functional. The above results suggest that it is rather difficult to predict the value of  $J_1$  in  $\text{Co}_3\text{O}_4$  from DFT calculations, as different functionals give rather varying results. However, it has been pointed out that it is important to include spin-orbit coupling (SOC) to fully understand the magnetic properties of  $\text{Co}_3\text{O}_4$ . To probe the effect of SOC, we also calculated the orbital moments on the Co ions. Thus, we performed PBE+SOC and PBE+U<sub>eff</sub>+SOC calculations. We found a substantial orbital moment on the  $\text{Co}^{2+}$  ions, amounting to  $0.16\mu_{\text{B}}$  for PBE+SOC and  $0.20\mu_{\text{B}}$  for PBE+U<sub>eff</sub>+SOC. Thus, the total moments are  $2.44\mu_{\text{B}}$  and  $2.91\mu_{\text{B}}$  using PBE+SOC and PBE+U<sub>eff</sub>+SOC, respectively. Surprisingly, the calculated values of  $J_1$  turn out to be positive, which indicate that the FM state is more stable than the AFM state, which is at odds with some experimental evidence.<sup>18</sup> In all cases without SOC, the FM state is higher in energy than the AFM state. However, there might be additional hidden magnetic structures present in the  $\text{Co}_3\text{O}_4$  (i.e., noncollinear magnetic structures where the direction of the spin quantization axis might be important), which will be the topic of future investigation.

#### 4. SUMMARY

In this work, we investigated the electronic, optical, and magnetic properties of the spinel compound  $\text{Co}_3\text{O}_4$  as well as its bonding scheme. We employed density functional theory at the PBE, PBE+U<sub>eff</sub>, and HSE06 levels as well as a many-body Green's function approach to resolve the long-standing problem of the correct band gap and electronic structure for this material. In addition to the band gap, we also calculated the imaginary part of the macroscopic dielectric function ( $\text{Im}(\epsilon)$ ), which is directly related to the absorption spectrum of  $\text{Co}_3\text{O}_4$ . Our calculations revealed that the electronic and magnetic properties of  $\text{Co}_3\text{O}_4$  are very sensitive to the choice of the Hubbard parameter (for PBE+U<sub>eff</sub>) and the amount of exact exchange included in the HSE06 hybrid functional. We compared the computed electronic structures of  $\text{Co}_3\text{O}_4$  with recently measured PES and UPS data.<sup>9,27</sup> Additionally, our calculated optical band gap is verified by recently measured absorption spectra and transient spectroscopy studies.<sup>9,34</sup> We found that the pure PBE functional, the hybrid HSE06 ( $\alpha = 5\%$ ) functional, and the Sc-GW0 method (full self-consistency over  $G$ ) are the most reliable methods for the electronic and optical properties of  $\text{Co}_3\text{O}_4$ . We conclude that the fundamental

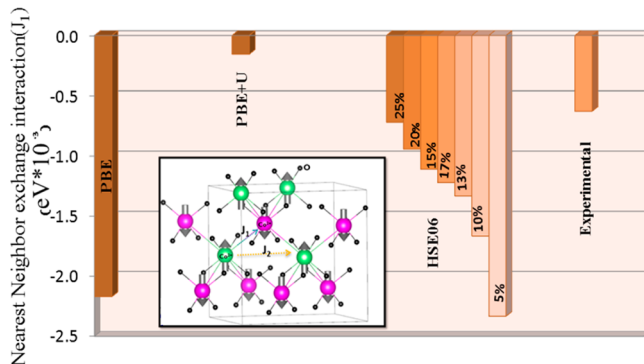


**Figure 6.** Experimental and calculated values of the nearest-neighbor exchange interaction parameter  $J_1$  for different DFT approaches for  $\text{Co}_3\text{O}_4$ . Negative  $J_1$  implies antiferromagnetic interactions.

exchange interaction theoretically, we calculated the nearest-neighbor exchange coupling parameter ( $J_1$ ) between  $\text{Co}^{2+}$  ions (Figure 6). We used a model proposed by Chen et al.<sup>22</sup> in which  $J_1$  is calculated from the difference between the total energy of the AFM and ferromagnetic (FM) configurations of the  $\text{Co}^{2+}$  ions. Thus, we considered the Heisenberg spin Hamiltonian  $\hat{H}_S$  shown in eq 1:

$$\hat{H}_S = - \sum_{ij} J_{ij} \hat{\mathbf{S}}_i \cdot \hat{\mathbf{S}}_j \quad (1)$$

band gap in  $\text{Co}_3\text{O}_4$  is direct with a value of ca. 0.8 eV. The present results may serve as a guide for the application of DFT methods to metal oxide materials, which are currently being explored in the emerging field of all-oxide photovoltaics.<sup>7</sup>

## ■ ASSOCIATED CONTENT

### Supporting Information

Bar diagram showing the variation of the energy band gap and partial density of states for various HSE06 screening parameters; variation in the energy band gap with respect to the percentage of exact exchange used in HSE06 calculations; partial density of states for  $\text{Co}_3\text{O}_4$  using the HSE06 functional with varying amounts of exact exchange; calculated  $\text{Im}(\epsilon)$  for different levels of DFT; total density of states obtained by G0W0 calculations using initial input from the PBE, PBE+ $U_{\text{eff}}$  and HSE06 ( $\alpha = 5\%$ ) functionals; calculated total band structures for all levels of GW; calculated partial density of states for all levels of GW calculations performed, with local field effects treated at the DFT and Hartree levels; calculated  $\text{Im}(\epsilon)$  for different levels of GW as functions of photon energy; and a table showing the calculated band gaps, band-gap types, and magnetic moments for all levels of GW. This material is available free of charge via the Internet at <http://pubs.acs.org>.

## ■ AUTHOR INFORMATION

### Corresponding Author

\*E-mail: majort@biu.ac.il.

### Funding

The authors acknowledge financial support from the Israeli National Nanotechnology Initiative (INNI) (FTA Project). M.K. acknowledges financial support from the Ministry of Absorption.

### Notes

The authors declare no competing financial interest.

## ■ REFERENCES

- O'Regan, B.; Grätzel, M. A low-cost, high-efficiency solar cell based on dye-sensitized colloidal  $\text{TiO}_2$  films. *Nature* **1991**, *353*, 737–740.
- Lewis, N. S. Toward Cost-Effective Solar Energy Use. *Science* **2007**, *315*, 798–801.
- Hagfeldt, A.; Boschloo, G.; Sun, L.; Kloo, L.; Pettersson, H. Dye-Sensitized Solar Cells. *Chem. Rev.* **2010**, *110*, 6595–6663.
- Rühle, S.; Shalom, M.; Zaban, A. Quantum-Dot-Sensitized Solar Cells. *ChemPhysChem* **2010**, *11*, 2290–2304.
- Nayak, P. K.; Bisquert, J.; Cahen, D. Assessing Possibilities and Limits for Solar Cells. *Adv. Mater.* **2011**, *23*, 2870–2876.
- Burschka, J.; Pellet, N.; Moon, S.-J.; Humphry-Baker, R.; Gao, P.; Nazeeruddin, M. K.; Grätzel, M. Sequential deposition as a route to high-performance perovskite-sensitized solar cells. *Nature* **2013**, *499*, 316–319.
- Rühle, S.; Anderson, A. Y.; Barad, H.-N.; Kupfer, B.; Bouhadana, Y.; Rosh-Hodesh, E.; Zaban, A. All-Oxide Photovoltaics. *J. Phys. Chem. Lett.* **2012**, *3*, 3755–3764.
- Anderson, A. Y.; Bouhadana, Y.; Barad, H.-N.; Kupfer, B.; Rosh-Hodesh, E.; Aviv, H.; Tischler, Y. R.; Rühle, S.; Zaban, A. Quantum Efficiency and Bandgap Analysis for Combinatorial Photovoltaics: Sorting Activity of Cu–O Compounds in All-Oxide Device Libraries. *ACS. Comb. Sci.* **2014**, *16*, 53–65.
- Qiao, L.; Xiao, H.; Meyer, H.; Sun, J.; Rouleau, C.; Puretzky, A.; Geohegan, D.; Ivanov, I.; Yoon, M.; Weber, W. Nature of the band gap and origin of the electro-/photo-activity of  $\text{Co}_3\text{O}_4$ . *J. Mater. Chem. C* **2013**, *1*, 4628–4633.
- Kupfer, B.; Majhi, K.; Keller, D. A.; Bouhadana, Y.; Ruhle, S.; Barad, H. N.; Anderson, A. Y.; Zaban, A. Thin Film  $\text{Co}_3\text{O}_4/\text{TiO}_2$  Heterojunction Solar Cells. *Adv. Energy Mater.* **2014**, DOI: 10.1002/aenm.201401007.
- Lou, X. W.; Deng, D.; Lee, J. Y.; Feng, J.; Archer, L. A. Self-Supported Formation of Needlelike  $\text{Co}_3\text{O}_4$  Nanotubes and Their Application as Lithium-Ion Battery Electrodes. *Adv. Mater.* **2008**, *20*, 258–262.
- Jiao, F.; Frei, H. Nanostructured Cobalt Oxide Clusters in Mesoporous Silica as Efficient Oxygen-Evolving Catalysts. *Angew. Chem., Int. Ed.* **2009**, *48*, 1841–1844.
- Gasparotto, A.; Barreca, D.; Bekermann, D.; Devi, A.; Fischer, R. A.; Fornasiero, P.; Gombac, V.; Lebedev, O. I.; Maccato, C.; Montini, T. F-doped  $\text{Co}_3\text{O}_4$  photocatalysts for sustainable  $\text{H}_2$  generation from water/ethanol. *J. Am. Chem. Soc.* **2011**, *133*, 19362–19365.
- Liang, Y.; Li, Y.; Wang, H.; Zhou, J.; Wang, J.; Regier, T.; Dai, H.  $\text{Co}_3\text{O}_4$  nanocrystals on graphene as a synergistic catalyst for oxygen reduction reaction. *Nat. Mater.* **2011**, *10*, 780–786.
- Liu, J.; Jiang, J.; Cheng, C.; Li, H.; Zhang, J.; Gong, H.; Fan, H. J.  $\text{Co}_3\text{O}_4$  Nanowire@ $\text{MnO}_2$  Ultrathin Nanosheet Core/Shell Arrays: A New Class of High-Performance Pseudocapacitive Materials. *Adv. Mater.* **2011**, *23*, 2076–2081.
- Paudel, T. R.; Zakutayev, A.; Lany, S.; d'Avezac, M.; Zunger, A. Doping Rules and Doping Prototypes in  $\text{A}_2\text{BO}_4$  Spinel Oxides. *Adv. Funct. Mater.* **2011**, *21*, 4493–4501.
- Xiao, X.; Liu, X.; Zhao, H.; Chen, D.; Liu, F.; Xiang, J.; Hu, Z.; Li, Y. Facile shape control of  $\text{Co}_3\text{O}_4$  and the effect of the crystal plane on electrochemical performance. *Adv. Mater.* **2012**, *24*, 5762–5766.
- Roth, W. L. The magnetic structure of  $\text{Co}_3\text{O}_4$ . *J. Phys. Chem. Solids* **1964**, *25*, 1–10.
- Kamimura, H. Nuclear Magnetic Resonance of Paramagnetic  $\text{Co}_3\text{O}_4$ . II. Theory of the NMR Shift. *J. Phys. Soc. Jpn.* **1966**, *21*, 484–490.
- Scheerlinck, D.; Hautecler, S. Magnetic interactions in  $\text{Co}_3\text{O}_4$ . *Phys. Status Solidi B* **1976**, *73*, 223–228.
- Walsh, A.; Wei, S.-H.; Yan, Y.; Al-Jassim, M.; Turner, J. A.; Woodhouse, M.; Parkinson, B. Structural, magnetic, and electronic properties of the Co–Fe–Al oxide spinel system: Density-functional theory calculations. *Phys. Rev. B* **2007**, *76*, No. 165119.
- Chen, J.; Wu, X.; Selloni, A. Electronic structure and bonding properties of cobalt oxide in the spinel structure. *Phys. Rev. B* **2011**, *83*, No. 245204.
- Zaanen, J.; Sawatzky, G.; Allen, J. Band gaps and electronic structure of transition-metal compounds. *Phys. Rev. Lett.* **1985**, *55*, 418–421.
- Sarma, D.; Krishnamurthy, H.; Nimkar, S.; Ramasesha, S.; Mitra, P. P.; Ramakrishnan, T. Electronic structure of high- $T_c$  superconductors and related compounds. *Pramana* **1992**, *38*, L531–L538.
- Arima, T.; Tokura, Y.; Torrance, J. Variation of optical gaps in perovskite-type 3d transition-metal oxides. *Phys. Rev. B* **1993**, *48*, 17006–17009.
- Chuang, T.; Brundle, C.; Rice, D. Interpretation of the X-ray photoemission spectra of cobalt oxides and cobalt oxide surfaces. *Surf. Sci.* **1976**, *59*, 413–429.
- Jugnet, Y.; Duc, T. M. Structure électronique des oxydes de cobalt  $\text{CoO}$  et  $\text{Co}_3\text{O}_4$ . *J. Phys. Chem. Solids* **1979**, *40*, 29–37.
- Tanaka, T. Optical Constants of Polycrystalline 3d Transition Metal Oxides in the Wavelength Region 350 to 1200 nm. *Jpn. J. Appl. Phys.* **1979**, *18*, 1043–1047.
- Belova, I. D.; Roginskaya, Y. E.; Shifrina, R. R.; Gagarin, S. G.; Plekhanov, Y. V.; Venetsev, Y. N. Co(III) ions high-spin configuration in nonstoichiometric  $\text{Co}_3\text{O}_4$  films. *Solid State Commun.* **1983**, *47*, 577–584.
- Cheng, C.-S.; Serizawa, M.; Sakata, H.; Hirayama, T. Electrical conductivity of  $\text{Co}_3\text{O}_4$  films prepared by chemical vapour deposition. *Mater. Chem. Phys.* **1998**, *53*, 225–230.
- Barreca, D.; Massignan, C.; Daolio, S.; Fabrizio, M.; Piccirillo, C.; Armelao, L.; Tondello, E. Composition and microstructure of cobalt oxide thin films obtained from a novel cobalt(II) precursor by chemical vapor deposition. *Chem. Mater.* **2001**, *13*, 588–593.

- (32) Martens, J. W. D.; Peeters, W. L.; van Noort, H. M.; Erman, M. Optical, magneto-optical and Mössbauer spectroscopy on  $\text{Co}^{3+}$  substituted cobalt ferrite  $\text{Co}^{2+}\text{Fe}_{2-x}\text{Co}_x^{3+}\text{O}_4$  ( $0 \leq x \leq 2$ ). *J. Phys. Chem. Solids* **1985**, *46*, 411–416.
- (33) Kim, K. J.; Park, Y. R. Optical investigation of charge-transfer transitions in spinel  $\text{Co}_3\text{O}_4$ . *Solid State Commun.* **2003**, *127*, 25–28.
- (34) Waegelé, M. M.; Doan, H. Q.; Cuk, T. Long-Lived Photoexcited Carrier Dynamics of d-d Excitations in Spinel Ordered  $\text{Co}_3\text{O}_4$ . *J. Phys. Chem. C* **2014**, *118*, 3426–3432.
- (35) Miedzinska, K.; Hollebone, B.; Cook, J. An assignment of the optical absorption spectrum of mixed valence  $\text{Co}_3\text{O}_4$  spinel films. *J. Phys. Chem. Solids* **1987**, *48*, 649–656.
- (36) Xu, X.-L.; Chen, Z.-H.; Li, Y.; Chen, W.-K.; Li, J.-Q. Bulk and surface properties of spinel  $\text{Co}_3\text{O}_4$  by density functional calculations. *Surf. Sci.* **2009**, *603*, 653–658.
- (37) Baerends, E.; Gritsenko, O.; Van Meer, R. The Kohn–Sham gap, the fundamental gap and the optical gap: The physical meaning of occupied and virtual Kohn–Sham orbital energies. *Phys. Chem. Chem. Phys.* **2013**, *15*, 16408–16425.
- (38) Lima, A. F. Interpretation of the optical absorption spectrum of  $\text{Co}_3\text{O}_4$  with normal spinel structure from first principles calculations. *J. Phys. Chem. Solids* **2014**, *75*, 148–152.
- (39) Li, W.; Walther, C. F.; Kuc, A.; Heine, T. Density functional theory and beyond for band-gap screening: Performance for transition-metal oxides and dichalcogenides. *J. Chem. Theory Comput.* **2013**, *9*, 2950–2958.
- (40) Aryasetiawan, F.; Gunnarsson, O. The GW method. *Rep. Prog. Phys.* **1998**, *61*, 237–312.
- (41) Kresse, G.; Hafner, J. Ab initio molecular dynamics for liquid metals. *Phys. Rev. B* **1993**, *47*, 558–561.
- (42) Blöchl, P. E. Projector augmented-wave method. *Phys. Rev. B* **1994**, *50*, 17953–17979.
- (43) Kresse, G.; Furthmüller, J. Efficient iterative schemes for ab initio total-energy calculations using a plane-wave basis set. *Phys. Rev. B* **1996**, *54*, 11169–11186.
- (44) Heyd, J.; Scuseria, G. E.; Ernzerhof, M. Hybrid functionals based on a screened Coulomb potential. *J. Chem. Phys.* **2003**, *118*, 8207–8215.
- (45) Blöchl, P. E.; Jepsen, O.; Andersen, O. K. Improved tetrahedron method for Brillouin-zone integrations. *Phys. Rev. B* **1994**, *49*, 16223–16233.
- (46) Cococcioni, M.; de Gironcoli, S. Linear response approach to the calculation of the effective interaction parameters in the LDA+U method. *Phys. Rev. B* **2005**, *71*, No. 035105.
- (47) Marques, M. A. L.; Vidal, J.; Oliveira, M. J. T.; Reining, L.; Botti, S. Density-based mixing parameter for hybrid functionals. *Phys. Rev. B* **2011**, *83*, No. 035119.
- (48) Kehoe, A. B.; Scanlon, D. O.; Watson, G. W. Nature of the band gap of  $\text{Ti}_2\text{O}_3$ . *Phys. Rev. B* **2011**, *83*, No. 233202.
- (49) Gajdoš, M.; Hummer, K.; Kresse, G.; Furthmüller, J.; Bechstedt, F. Linear optical properties in the projector-augmented wave methodology. *Phys. Rev. B* **2006**, *73*, No. 045112.
- (50) Aguilera, I.; Vidal, J.; Wahón, P.; Reining, L.; Botti, S. First-principles study of the band structure and optical absorption of  $\text{CuGaS}_2$ . *Phys. Rev. B* **2011**, *84*, No. 085145.
- (51) Liao, P.; Carter, E. A. Testing variations of the GW approximation on strongly correlated transition metal oxides: Hematite ( $\alpha\text{-Fe}_2\text{O}_3$ ) as a benchmark. *Phys. Chem. Chem. Phys.* **2011**, *13*, 15189–15199.
- (52) Dronskowski, R.; Blöchl, P. E. Crystal orbital Hamilton populations (COHP): Energy-resolved visualization of chemical bonding in solids based on density-functional calculations. *J. Phys. Chem. B* **1993**, *97*, 8617–8624.
- (53) Deringer, V. L.; Tchougréeff, A. L.; Dronskowski, R. Crystal Orbital Hamilton Population (COHP) Analysis As Projected from Plane-Wave Basis Sets. *J. Phys. Chem. A* **2011**, *115*, 5461–5466.
- (54) Maintz, S.; Deringer, V. L.; Tchougréeff, A. L.; Dronskowski, R. Analytic projection from plane-wave and PAW wavefunctions and application to chemical-bonding analysis in solids. *J. Comput. Chem.* **2013**, *34*, 2557–2567.
- (55) Jana, S.; Singh, V.; Nag, A.; Meneghini, C.; Dasgupta, I.; Aquilanti, G.; Ray, S.  $\text{LaSrVMoO}_6$ : A case study for A-site covalency-driven local cationic order in double perovskites. *Phys. Rev. B* **2012**, *86*, No. 014203.
- (56) Onida, G.; Reining, L.; Rubio, A. Electronic excitations: Density-functional versus many-body Green's-function approaches. *Rev. Mod. Phys.* **2002**, *74*, 601–659.
- (57) van Schilfgaarde, M.; Kotani, T.; Faleev, S. Quasiparticle Self-Consistent GW Theory. *Phys. Rev. Lett.* **2006**, *96*, No. 226402.
- (58) Shishkin, M.; Kresse, G. Self-consistent GW calculations for semiconductors and insulators. *Phys. Rev. B* **2007**, *75*, No. 235102.
- (59) Toroker, M. C.; Kanan, D. K.; Alidoust, N.; Isseroff, L. Y.; Liao, P.; Carter, E. A. First principles scheme to evaluate band edge positions in potential transition metal oxide photocatalysts and photoelectrodes. *Phys. Chem. Chem. Phys.* **2011**, *13*, 16644–16654.
- (60) Caruso, F.; Rinke, P.; Ren, X.; Scheffler, M.; Rubio, A. Unified description of ground and excited states of finite systems: The self-consistent GW approach. *Phys. Rev. B* **2012**, *86*, No. 081102.
- (61) von Barth, U.; Holm, B. Self-consistent  $GW_0$  results for the electron gas: Fixed screened potential  $W_0$  within the random-phase approximation. *Phys. Rev. B* **1996**, *54*, 8411–8419.
- (62) Holm, B.; von Barth, U. Fully self-consistent GW self-energy of the electron gas. *Phys. Rev. B* **1998**, *57*, 2108–2117.
- (63) Kotani, T.; van Schilfgaarde, M.; Faleev, S. V.; Chantis, A. Quasiparticle self-consistent GW method: A short summary. *J. Phys.: Condens. Matter* **2007**, *19*, No. 365236.
- (64) Marom, N.; Caruso, F.; Ren, X.; Hofmann, O. T.; Körzdörfer, T.; Chelikowsky, J. R.; Rubio, A.; Scheffler, M.; Rinke, P. Benchmark of GW methods for azabenzenes. *Phys. Rev. B* **2012**, *86*, No. 245127.
- (65) Hamann, D.; Vanderbilt, D. Maximally localized Wannier functions for GW quasiparticles. *Phys. Rev. B* **2009**, *79*, No. 045109.
- (66) Hautier, G.; Miglio, A.; Ceder, G.; Rignanese, G.-M.; Gonze, X. Identification and design principles of low hole effective mass p-type transparent conducting oxides. *Nat. Commun.* **2013**, *4*, No. 2292.
- (67) Perdew, J. P. Density functional theory and the band gap problem. *Int. J. Quantum Chem.* **1985**, *28*, 497–523.
- (68) Perdew, J. P.; Burke, K.; Ernzerhof, M. Generalized gradient approximation made simple. *Phys. Rev. Lett.* **1996**, *77*, 3865–3868.
- (69) Lucero, M.; Henderson, T. M.; Scuseria, G. Improved semiconductor lattice parameters and band gaps from a middle-range screened hybrid exchange functional. *J. Phys.: Condens. Matter* **2012**, *24*, No. 145504.
- (70) Dudarev, S. L.; Botton, G. A.; Savrasov, S. Y.; Humphreys, C. J.; Sutton, A. P. Electron-energy-loss spectra and the structural stability of nickel oxide: An LSDA+U study. *Phys. Rev. B* **1998**, *57*, 1505–1509.
- (71) Perdew, J. P.; Ernzerhof, M.; Burke, K. Rationale for mixing exact exchange with density functional approximations. *J. Chem. Phys.* **1996**, *105*, 9982–9985.
- (72) Scheerlinck, D.; Hautecler, S.; Wegener, W. Exchange integral determination in  $\text{Co}_3\text{O}_4$ . *Phys. Status Solidi B* **1975**, *68*, 535–541.